

Experimental Characterization and Statistical Analysis of Water-Based Gold Nanofluids for Solar Applications: Optical Properties and Photothermal Conversion Efficiency

Jorge Burgos, Rosa Mondragón, Elif Begum Elcioglu, Francisco Fabregat-Santiago, and Leonor Hernández*

Optimizing optical and photothermal properties of the solar nanofluids (NFs) to be used in direct absorption solar collectors is a key issue to maximize efficiencies in these collector types. This work both experimentally and statistically analyzes the influence of the size (5 and 20 nm) and concentration (5.1, 28.2, and 51.3 ppm) of gold nanoparticles (NPs) on several important variables for collector performance: NF stability, extinction coefficient, photothermal efficiency, etc. The research work shows that the addition of small amounts of gold NPs, whose surface plasmon resonance has wavelengths close to 520 nm, greatly improves the light absorption capacity of the base fluid (water). The statistical analysis confirms the influence of NP size and concentration on photothermal conversion efficiency (PTE), which lead to an increase of up to 121% for the smallest-sized NF with the highest concentration.


1. Introduction

The 2015 Paris Agreement was motivated to obtain a global response to climate change by keeping the rise in global temperature well below 2 °C and pursuing efforts to limit it to 1.5 °C.^[1] European Union and United Nations Member States intend to address different strategies in relation to the energy system: improving energy efficiency and decarbonizing energy production systems by implementing renewable energy sources.

J. Burgos, R. Mondragón, L. Hernández
Departamento de Ingeniería Mecánica y Construcción
Universitat Jaume I
12071 Castellón de la Plana, Spain
E-mail: lhernand@uji.es

E. B. Elcioglu
Department of Mechanical Engineering
Eskisehir Technical University
26555 Eskisehir, Turkey

F. Fabregat-Santiago
Institute of Advanced Materials (INAM)
Universitat Jaume I
12071 Castellón de la Plana, Spain

 The ORCID identification number(s) for the author(s) of this article can be found under <https://doi.org/10.1002/solr.202200104>.

© 2022 The Authors. Solar RRL published by Wiley-VCH GmbH. This is an open access article under the terms of the Creative Commons Attribution-NonCommercial-NoDerivs License, which permits use and distribution in any medium, provided the original work is properly cited, the use is non-commercial and no modifications or adaptations are made.

DOI: 10.1002/solr.202200104

While recent trends indicate that the implementation of environment-conscious energy systems is an accompanist to alternative fossil fuel use, it is becoming increasingly clear that a paradigm change is required to make clean energy processes dominant to not exceed the global warming limit.

In recent decades, solar energy has been regarded as the most promising source of inexhaustible clean energy. The two main ways of collecting and transforming solar energy are photovoltaic solar energy and solar thermal energy,^[2] of which the latter is the basis of this work. In solar thermal energy, solar radiation is collected by an absorption material and transferred as heat

energy to a transfer medium, usually a heat transfer fluid (HTF). Solar collectors are the devices used for solar-to-thermal energy conversion. They can be classified as concentrating and non-concentrating solar collectors. Non-concentrating solar collectors are used at low-to-medium temperatures, while the concentrating collectors that employ mirrors to concentrate incident solar energy are employed at higher temperatures.

The absorption material in conventional collectors is a dark surface that heats up and transfers heat to the HTF flowing through pipes. Although these collectors offer good energy conversion efficiency, a series of thermal losses appear to lower the possible maximum efficiency limit. In the 1970s, directly exposing HTF to incident radiation was proposed as an alternative to avoid such losses in conventional collectors.^[3] This concept, in which heat is absorbed volumetrically by the working fluid instead of the surface, is known as direct absorption solar collectors (DASC). However, commonly used HTFs (water, oils, molten salts, etc.) are transparent in most of the solar spectrum, possess low solar radiation absorption capacity and, hence, offer low solar-to-thermal conversion efficiency. To overcome this issue, nanofluids (NFs) used as HTFs have been proposed in the literature.^[4]

NFs were first postulated by Choi in 1995^[5] as suspensions of nanoparticles (NPs, with sizes ranging from 1 to 100 nm) homogeneously dispersed in a base fluid to achieve improved thermal properties, mainly thermal conductivity and heat transfer performance. A wide variety of materials of different natures can be employed in these NFs to improve thermal characteristics. Some examples are metals (Ag, Au, Cu, Al, etc.), metal oxides (SiO₂, Al₂O₃, TiO₂, CuO, Fe₂O₃, etc.), and carbon-based materials (carbon nanotubes, graphene, graphene oxide, graphite, etc.).^[6–9]

The term solar NFs was later proposed in 2009 by Otanicar et al.^[10] It refers to those NFs with better solar radiation absorption capacity thanks to the addition of NPs, even at very low concentrations.^[11,12] Since then, many works have studied the optical properties and photothermal conversion efficiency (PTE) of solar NFs. This consists of different NPs like metals,^[13–23] metal oxides,^[24–26] carbon-based materials,^[27–30] and hybrid composites.^[31–33] The NFs from coffee waste or black Chinese ink^[34–36] have been investigated as possible NFs for being cheap and also biodegradable. Hence they can reduce waste production.

Metal NPs include a special group of metals of much interest as solar NFs because they exhibit surface plasmon resonance (SPR) at certain wavelengths when exposed to sunlight. They also have the potential to enhance absorption characteristics.^[37] This plasmonic response is a collective oscillation of electrons, stimulated by incident light absorption. It is an effective way of increasing solar energy in thermal energy conversion. Therefore, these NPs are interesting candidates for the photothermal conversion processes required in DASCs. The metal NPs that present SPR include Au, Ag, Cu, Al, and Li. Of these, Ag, Cu, and Al are easily oxidized, and Li is difficult to handle given its reactivity. Au NPs exhibit good colloidal and thermal stability, high electrical and thermal conductivity, and strong SPR over a wide wavelength range within the sunlight spectrum, all of which make it a good candidate as an NP in solar NFs for DASC.

A parameter-based review literature is presented in Table 1. It summarizes the results obtained in previous works for PTE. PTE is defined as the ratio between the energy absorbed by the NF to the incident radiation for pure water and water-based Au NFs with different NP sizes and concentrations.

Table 1 reveals how PTE values differ depending on the energy source, radiation conditions, and NF characteristics, with values ranging from 8% to 71% for pure water. PTE is always enhanced when Au NPs are added, even at very low concentrations. Enhancements from 11%^[18] to 518%^[20] have been reported for different tested conditions. These findings reflect the high

potential of Au NPs for solar-to-thermal conversion processes under optimal conditions.

A statistical analysis is an important and rather recently appreciated requirement for the NFs productization path for enabling: 1) evaluations of parameter (e.g., NP concentration and morphology, temperature, NF type) effects on performance (e.g., thermal efficiency); 2) evaluations of associations (correlations) between parameters (e.g., between NP agglomeration and viscosity); and 3) performance predictions (e.g., Nusselt number correlations, figures of merit); and all quantitatively.^[38] Accordingly, this work employs statistical analyses to quantify: 1) whether a dependent variable changes significantly as an independent variable change; and 2) how parameters are associated with or correlate to one another.

In this article, the optical and photothermal properties of NFs were studied in-depth for aqueous Au NFs. The results were compared to pure water. The morphology and colloidal stability of NPs in the fluid were analyzed by transmission electron microscopy (TEM) and the dynamic light scattering (DLS) technique. The influence of both NP size (5 and 20 nm) and concentration (51.3, 28.2, and 5.1 ppm) on optical and photothermal properties (i.e., extinction coefficient, fraction of absorbed sunlight, temperature increase, and PTE) was experimentally studied. The experimental data were processed by rigorous statistical analyses to quantitatively interpret the results and to shed light on statistically significant variations and associations.

2. Experimental Section

2.1. NFs and Experimental Conditions

The two selected commercial Au NFs (particle sizes 5 and 20 nm) were supplied by Sigma-Aldrich. Both were stabilized in 0.1 mM phosphate-buffered saline (PBS). Micrographs of both the 5 and 20 nm NPs appear in Section 3.1 (Figure 4). Their optical density was 1 and they were free of reactants. Both commercial NFs were initially tested by inductively coupled plasma mass spectrometry

Table 1. Review of the PTE results for water-based gold NFs.

Author (year) [Ref]	Size [nm]	NP concentration [ppm]	Energy source ^{a)}	PTE _{water} [%]	PTE _{nf} [%]
Zhang et al. (2014, 2015) ^[14,16]	10–20	0.28–11.2	SS: 1000 W m ⁻²	45	54–78
Chen et al. (2016) ^[17]	10	0.5–2.5	SS:10 000 W m ⁻²	N/A	15–35
Chen et al. (2016) ^[18]	25, 33 and 40	0.08	SS: 450 W m ⁻²	Cube: 71 Flat: 65	Cube: 83.5–86.5 Flat: 72–85
Jin et al. (2016) ^[19]	20	0.36–5.8	NL:600–950 W m ⁻²	35 (@600 W m ⁻²) 17.3 (@950 W m ⁻²)	56–80 (@600 W m ⁻²) 45.5–73.6 (@950 W m ⁻²)
Jin et al. (2016) ^[20]	20	1.02–12.75	NL: Fresnel lens 220 000 W m ⁻²	13	45–80.3
Chen et al. (2017) ^[21]	10	0.5–2.5	SS: 10 000 W m ⁻²	N/A	48–70
Wang et al. (2017) ^[22]	13	5–178	SS: 10 000 W m ⁻²	8	19–25
He et al. (2018) ^[23]	10	5.1	SS: 1 mW μm ⁻²	33.8	71.7
Zeiny et al. (2018) ^[15]	3–6	30–150	SS:1000 W m ⁻²	23	28–44

^{a)}SS: Solar Simulator; NL: Natural Light.

Table 2. Test samples: nomenclature and experimental conditions.

ID	D [nm]	[Au] [ppm]
Water	0	0
5_5	5	5.1
5_28	5	28.2
5_51	5	51.3
20_5	20	5.1
20_28	20	28.2
20_51	20	51.3

(ICP-MS). The Au concentrations of 63.8 and 51.3 ppm for the 5 and 20 nm NFs were, respectively, obtained.

Table 2 and **Figure 1** include the nomenclature and conditions of the different samples tested in this study. The two independent variables of this experiment are NP diameter (D) and concentration ([Au]), respectively, at two and three levels. Concentrations were set at 51.3, 28.2, and 5.1 ppm for each NP size by diluting the initial commercial samples with distilled water. These two inputs were used to study their effect on the three following output (performance) variables: temperature variation (ΔT); PTE; distance at which 50% of incident solar radiation is absorbed (x_{50}).

2.2. Experimental Techniques

2.2.1. NP Concentration

The concentration of the NPs contained in NFs was measured by ICP-MS with an ICAP-RQ (ThermoFisher Scientific) device. Argon was the carrier gas. Helium was used to eliminate possible interferences. The sample volume was 10–15 mL and a gold standard was employed.

2.2.2. NP Morphology and Size, D

The Au NPs were observed under a transmission electron microscope (TEM, JEM-1010, JEOL) operating at an accelerating voltage of 100 kV, a resolution of 0.45 nm, and an AMT RX80 (8 Mpx) digital camera. A droplet of the NF was dispersed on a carbon-coated copper-based grid. The liquid content was removed with the help of absorbent paper to leave solid particles



Figure 1. Visual observation of the tested samples.

on the grid surface. Both morphology and primary particle size were studied with the acquired images.

The size distribution of the NPs in NF was analyzed by the DLS technique with a Zetasizer Nano ZS instrument (Malvern Instruments Ltd.). Size can be known from the light scattered by particles due to their Brownian motion and signal intensity. The equipment comprises a laser centered at 532 nm and a detector that acquires the intensity of the light scattered by suspended particles. Both the laser and detector are enclosed in the device. The hydrodynamic diameter is calculated based on the intensity of scattered light at 173°. It also contains a Peltier heating system that can heat samples up to 90 °C.

2.2.3. Thermal Conductivity, k

Samples' thermal conductivity was measured by the transient hot-wire technique using a TEMPOS conductimeter (Meter). The sample was placed inside a sealed glass tube (40 mL) where the sensor was vertically inserted. To run the test at a specific temperature, the tube was immersed in a thermostatic bath at a controlled temperature. Measurements were taken at 25 and 60 °C. Six tests were run for all the samples to obtain a mean value per temperature. The experimental error, ϵ , was obtained from the standard deviation, σ , of the n measurement taken

$$\epsilon = t_{n-1,0.025} \frac{\sigma}{\sqrt{n}} \quad (1)$$

where $t_{n-1,0.025}$ is the student's t -distribution for $n-1$ of freedom at the 95% confidence level. The average value of the relative experimental error for thermal conductivity was 2.64%.

2.2.4. Extinction Coefficient, $\mu_{\text{ext}}(\lambda)$

The extinction coefficient was estimated from optical measurements with a Lambda 1050 + UV/Vis/NIR (PerkinElmer) spectrophotometer. The system consists of a lamp as a light source, a mirror to produce a double beam, and two photodetectors located once the light has crossed the reference and sample cuvettes. The wavelength range of measurements spanned 220–1100 nm, which covers 83.5% of total solar radiation.

The spectral extinction coefficient ($\mu_{\text{ext}}(\lambda)$) was obtained according to the Beer–Lambert law, given by Equation (2). See the supporting information for more details

$$\mu_{\text{ext}}(\lambda) = -\frac{\log(T(\lambda))}{x} \quad (2)$$

where $T(\lambda)$ is spectral transmittance (the ratio between transmitted light and incident radiation) and x is the path length that equals sample thickness (namely 10 mm).

2.2.5. Sunlight-Absorbed Fraction, $F(x)$

The solar absorption ability of NFs is important in volumetric solar collectors and is evaluated by the sunlight-absorbed fraction $F(x)$. This parameter calculates the fraction of incident sunlight, $I_S(\lambda)$, which is absorbed by fluid after a penetration distance x

within the specified wavelength range. The $F(x)$ value is obtained by Equation (3)^[12,39,40]

$$F(x) = 1 - \frac{\int_{\lambda_{\min}}^{\lambda_{\max}} I_S(\lambda) \cdot e^{-\mu_{\text{ext}}(\lambda) \cdot x} d\lambda}{\int_{\lambda_{\min}}^{\lambda_{\max}} I_S(\lambda) d\lambda} \quad (3)$$

where $I_S(\lambda)$ was obtained from American Society for Testing and Materials solar radiation,^[41] the extinction coefficient was calculated by Equation (2) and the spectral range was determined by optical measurements (within $\lambda_{\min} = 220$ nm and $\lambda_{\max} = 1100$ nm). As a characteristic value for each sample, the penetration distance at which 50% of the incident radiation was absorbed (x_{50}) was determined.

2.2.6. Photothermal Conversion Efficiency

The measurements to determine the efficiency of fluids to transform solar energy into thermal energy were taken according to the experimental setup shown in Figure 2. It consisted of a quartz glass tube in which a 10 mL sample volume was placed per measurement. The quartz glass tube in the experiment was custom-made for high-temperature resistance purposes. The tube contained a vacuum interlayer to reduce heat losses by convection to ambient air. Fluids were placed inside the inner tube (25 mm diameter, 150 mm length). The outer-tube diameter was 50 mm. Samples' temperature evolution was recorded by a data acquisition system that comprised a data logger (Agilent 34 970 A) linked to a PC. As shown in Figure 2, a k-type thermocouple (RS PRO K-228-7451) with ± 1.5 °C measurement uncertainty was placed inside the fluid. This position remained constant in relation to the light source while taking all the measurements. Another thermocouple was employed to measure ambient temperature.

Samples were illuminated using a collimated radiation source from an artificial sunlight simulator (Oriel 6263 75 W Xe OZONE FREE). The spectrum of the source is depicted in Figure 3, which shows that the sunlight simulator reproduced to a certain extent the spectral behavior of solar irradiance at ground level, $I_S(\lambda)$. A potentiometer (Ophir 1Z01500, Nova

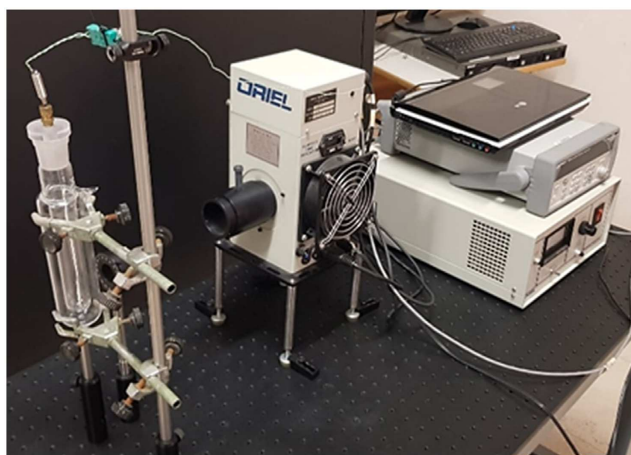


Figure 2. Experimental setup for the PTE tests.

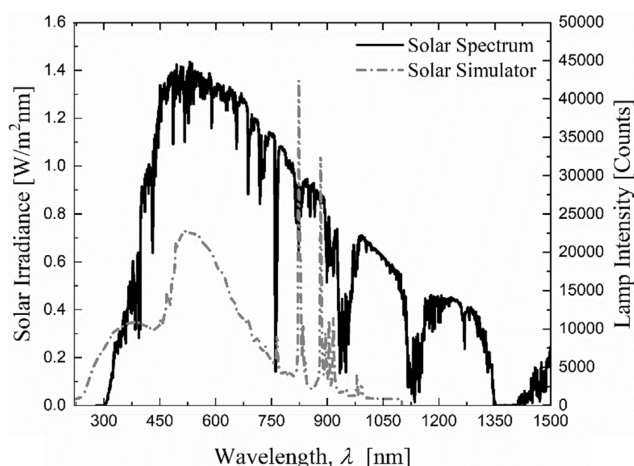


Figure 3. The solar (solid line) and artificial sunlight simulator (dashed line) spectra.

Display) was used to measure the solar simulator power in the quartz glass tube position (W_{measured}).

Experiments were performed in a closed insulated room to avoid thermal effects from the environment and to work under controlled conditions. Up to four repetitions of measurements were taken per sample to perform the statistical analysis.

PTE, as defined in Equation (4), was calculated as the ratio between the power of energy absorbed by fluid (W_{abs}) and the power of the incident radiation on the sample (W_{incident})

$$PTE = \frac{W_{\text{abs}}}{W_{\text{incident}}} = \frac{W_{\text{abs}}}{W_{\text{measured}} \cdot \tau} \quad (4)$$

where W_{incident} was calculated by applying a correction factor, τ , to the potentiometer measurement (W_{measured}). This factor considers the losses brought about by light propagating through media with different refractive indexes, including air, quartz, vacuum, and fluid. In this work, its value was 0.86.^[42]

Two different methods were followed to estimate PTE. The first method (Equation (5)), evaluates W_{abs} as the energy stored in fluid and does not take heat losses into account

$$PTE_1 = \frac{W_{\text{abs}}}{W_{\text{measured}} \cdot \tau} = \frac{(c_{p,w} \cdot m_w + c_{p,np} \cdot m_{np}) \cdot \Delta T}{W_{\text{measured}} \cdot \tau \cdot \Delta t} \sim \frac{(c_{p,w} \cdot m_w) \cdot \Delta T}{W_{\text{measured}} \cdot \tau \cdot \Delta t} \quad (5)$$

where $c_{p,w}$, m_w and $c_{p,np}$, m_{np} are, respectively, the specific heat, mass of water, and the NP. ΔT is the temperature increase within a time interval Δt . As the NP concentration of the NF was very low, term $(c_{p,np} \cdot m_{np})$ was disregarded.^[16,19,21] Enough time was left for the experimental temperature to stabilize. So PTE₁ was calculated for 5400 s.

To calculate the power absorbed by fluid in the second method, W_{abs} , a balance was struck between the power measured directly in fluid, W_{sample} , and the power associated with losses due to convection and heat radiation effects, W_{loss} , by these equations

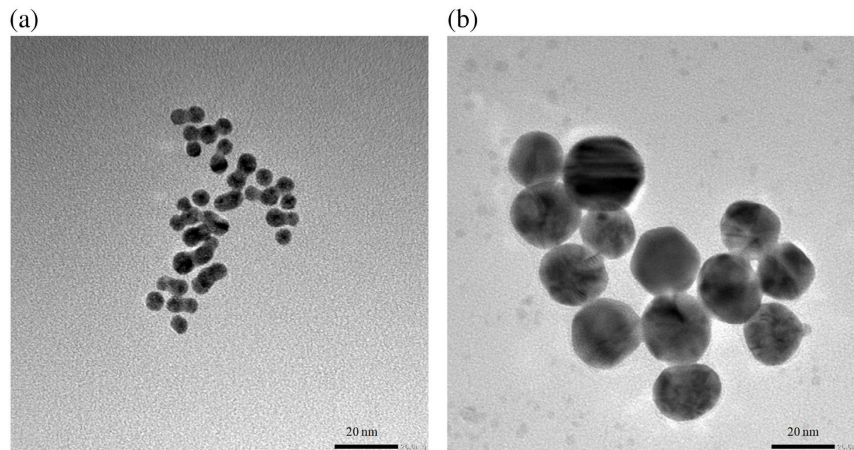


Figure 4. Gold NPs: a) 5 nm and b) 20 nm.

$$W_{\text{sample}} = W_{\text{abs}} - W_{\text{loss}} \quad (6)$$

$$m_w \cdot c_{p,w} \cdot \frac{dT}{dt} = W_{\text{abs}} - \beta(T - T_a) \quad (7)$$

where T is fluid temperature, T_a is ambient temperature and β is the loss coefficient. In this case, the NP contribution to the W_{sample} term was neglected. By operating and applying the experiment's boundary conditions, the equation of the heating process can be obtained

$$T = \left[\frac{W_{\text{abs}}}{\beta} + T_a \right] + \left[T_0 - T_a - \frac{W_{\text{abs}}}{\beta} \right] e^{-\frac{\beta}{m_w \cdot c_{p,w}} \cdot t} \quad (8)$$

where T_0 is the initial NF temperature and t is time (also 5400 s in this case). By fitting the measured temperature to the theoretical exponential curve in Equation (8), W_{abs} was obtained. Therefore, PTE₂ was calculated using Equation (4).

3. Results and Discussion

3.1. NP Size and Colloidal Stability

The morphology and size of the primary NPs dispersed in the commercial NFs were observed by TEM as received. The micrographs of both materials are shown in **Figure 4**. It depicts how particles were almost spherical in shape. The primary particle size well agreed with the values provided by the manufacturer.

To analyze the degree of dispersion of the NPs in the base fluid and its colloidal stability with temperature increase, DLS measurements of the two commercial NFs were taken between 25 and 60 °C. Tests were run for the highest NP concentration after checking that the influence of the solid content on particle size distribution was negligible. Figure S1, Supporting Information, offers the DSL results for the commercial and for all the diluted samples. The study of colloidal stability with temperature was then performed with the commercial NFs for being the most concentrated. As their stability was confirmed, further dilutions at lower concentrations were assumed stable.

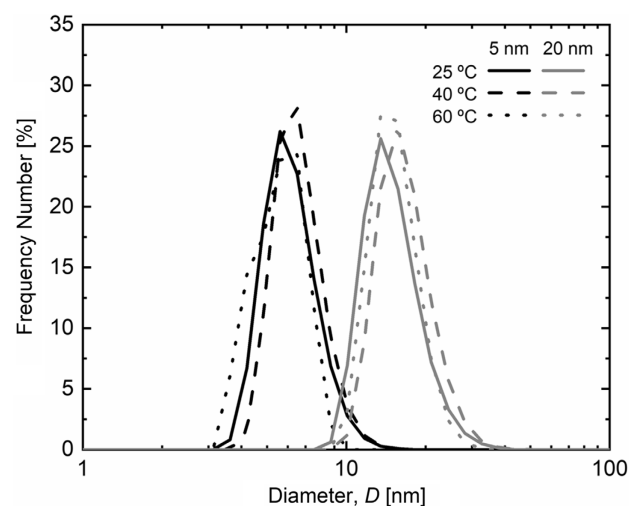


Figure 5. Evolution of particle size distribution with a temperature of the commercial NFs of 5 nm and 20 nm Au nanoparticles (NPs).

Table 3. Evolution of the mean particle size with temperature of the commercial NFs.

Temperature [°C]	D_{50} [nm]	
	5 [nm]	20 [nm]
25	6.0	16.2
40	7.3	18.9
60	5.8	16.5

The evolution of the particle size distributions obtained for both NFs with temperature appears in **Figure 5**. All the samples exhibited mono-modal distributions, and no large agglomerates formed in fluid. The mean diameter (D_{50}) values of the NPs for each temperature are included in **Table 3**. The results showed that the mean particle sizes came close to those of the manufacturer, and to those observed for the primary particles in the TEM

Table 4. Thermal conductivity enhancement at 25 and 60 °C.

Sample	Δk [%]	
	25 °C	60 °C
5_5	1.7	3.9
5_28	3.2	3.3
5_51	3.2	2.4
20_5	0.5	3.7
20_28	1.0	1.3
20_51	0.4	0.3

images, which corroborated NPs' high degree of dispersion. With the rising temperature, NPs remained mono-modal with a similar mean particle size, and displayed slight differences that could be attributed to the experimental error. These results indicate good colloidal stability with temperature for NFs with both NPs.

3.2. Thermal Conductivity

This section evaluates the thermal conductivity enhancement caused by adding solid particles to water. However, it should be noted that the NFs herein studied have very low particle concentrations. So limited increments were expected in this case. The results of the enhancements in relation to the base fluid are shown in **Table 4** for the six samples at 25 and 60 °C. In all cases, thermal conductivity increased when the Au NPs were present in the base fluid. The average enhancement was 2.08%. However, the obtained results indicate experimental uncertainty, and their difficult interpretation increases insofar as NP size or concentration are not feasible.

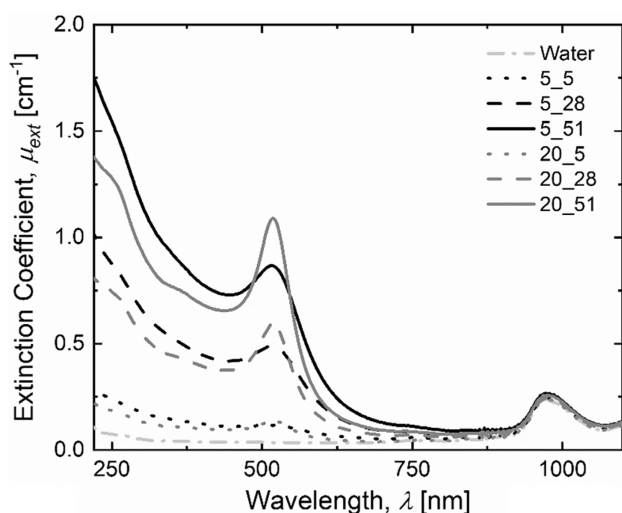


Figure 6. Extinction coefficient of the base fluid (water) and the water-based Au nanofluids (NFs).

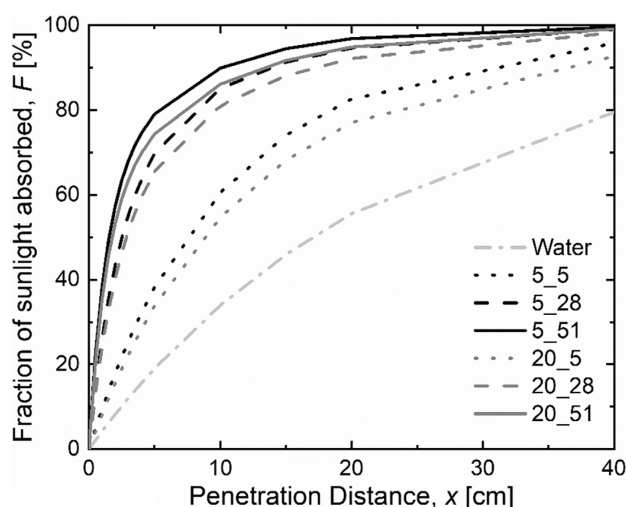


Figure 7. Fraction of absorbed sunlight in relation to the penetration distance of the base fluid (water) and the water-based Au NFs.

3.3. Optical Characterization

Figure 6 shows the extinction coefficients of the base fluid (water) and the water-based Au NFs with different NP sizes and concentrations. Water remained almost transparent over the entire studied wavelength range, and only a small amount of near-infrared light was absorbed. The extinction properties of NFs were enhanced given the presence of Au NPs. The peaks associated with the SPR of the Au NPs were located at 516 and 520 nm for the 5 and 20 nm samples, respectively, regardless of NP concentration. The peak wavelengths and the slight shift to longer wavelengths with particle size agreed with the values expected for the spherical Au NPs within this size range.^[14,15,18] Higher extinction coefficient magnitudes were obtained for the Au NFs with increasing concentrations. This means that as the sample became more concentrated, its absorption capability improved. The extinction coefficient for wavelengths below 450 nm lowered with increasing particle size, while within SPR wavelength ranges an increase is observed with particle size.

Figure 7 compares the fraction of sunlight absorbed by the tested samples ($F(x)$), as calculated with Equation (3). The obtained results clearly showed that using water-based Au NFs for a solar collector allowed sunlight to be fully absorbed at a shorter penetration distance compared to the base fluid

Table 5. Values of x_{50} and PTE for the different tested samples.

Sample ID	x_{50} [cm]	PTE ₁ [%]	PTE ₂ [%]
water	17.14	5.25	22.39
5_5	7.60	7.09	28.46
5_28	2.50	10.98	48.59
5_51	1.55	11.15	49.44
20_5	8.90	7.18	28.19
20_28	2.85	9.72	41.04
20_51	1.78	10.59	44.49

alone. Therefore, implementing NFs in a solar collector is expected to improve its compactness by reducing both the volume of required liquid and the system's cost. To quantitatively evaluate the differences in Figure 7, the values of the penetration distance at which the tested fluids absorbed 50% of the incident radiation (x_{50}) are shown in Table 5. The base fluid absorbed 50% of the incident radiation at a distance of 17.14 cm. The measured water-based Au NF with the highest concentration and the smallest NP size significantly cut this distance to 1.55 cm. This confirmed the positive effect of NPs' optical characteristics for efficient solar energy absorption.

Although optical properties are a key factor for evaluating solar NFs, detailed studies into photothermal conversion are necessary to better evaluate their applicability in DASC.

3.4. Photothermal Conversion Efficiency

To evaluate the efficiency to transform radiation from the solar simulator into heat, the temperature evolution with time in the different samples was measured from the experimental setup shown in Figure 2. After an initial rapid increase in temperature, a balance between heat losses and the energy of incident radiation was achieved, and provided a maximum temperature increase (see Figure 8). The water-based Au NFs showed a more marked temperature rise than that with water, which was expected given their corresponding extinction coefficients. For each NP size, ΔT increased as NP concentration rose. The maximum temperature increase obtained for water was 5.45 °C, while after adding gold NPs went up to 11.41 °C.

Both experimental PTEs were obtained from the measured temperature evolutions. Table 5 summarizes relevant data from each sample, including the penetration distance at which 50% of incident radiation was absorbed (x_{50}) and the experimental PTE obtained by both methods (PTE₁ and PTE₂). For PTE, the average values of all the repetitions for each sample are shown.

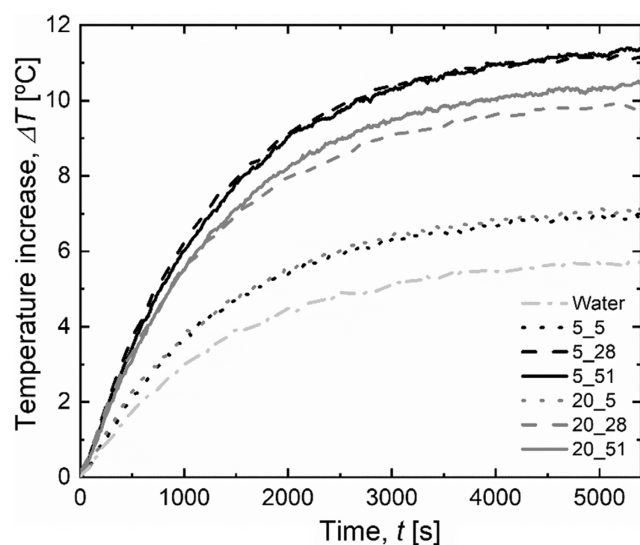


Figure 8. Temperature evolution of the base fluid (water) and the water-based Au NFs in relation to irradiation time.

Comparing the obtained PTE results to previous studies is not straightforward. Even for water, differences in experimental setups, selecting times for PTE calculations (5400 s in this study, but 300 s for Jin et al.^[20] and 60 s for Zhang et al.^[14]) and the PTE equations, can lead to a wide range of PTE values. Table 1 shows the PTE values for water within the 8–71% range. In this study, and depending on the PTE equations, the PTE value for water was 5.25% when heat losses were not contemplated and was 22.39% when they were.

By comparing the PTE values in Table 5 for all the samples, and as expected from the power balance equation, the photothermal conversion efficiencies that considered heat losses in the system (PTE₂) were higher than those that lacked them (PTE₁). According to Equation (5), as the sample mass remained constant in all the experiments, PTE₁ was directly proportional to the maximum temperature increase (ΔT) (see Figure 8). It is noteworthy that remarkable PTE values for the Au NFs were obtained even for very low NP concentrations.

A wide range of results has been reported by different studies for absolute PTE values. Thus to remove the influence of factors other than NP, it is better to analyze improvements in NFs in relation to the base fluid. Figure 9 includes the PTE enhancements provided by the NFs in Table 5 in relation to water, as calculated by Equation (9)

$$\text{Enhancement} = \frac{PTE_{nf} - PTE_w}{PTE_w} \cdot 100 \quad (9)$$

Although the absolute values obtained for both PTE definitions differed, the enhancements provided by both equations indicated similar trends. As observed in Figure 9 for both experimental PTEs, the higher the NP concentration, the greater the PTE. Although this relation was not linear, a rapid increase was noted for both NP sizes when changing from 5.1 to 28.2 ppm, with somewhat asymptotic behavior when moving to the highest concentration. This could be related to the fluid thickness effect, where the absorption efficiency of an NP may vary with fluid depth.^[14,18,22] The maximum enhancement was around 121% for the sample with the smallest particle size and the highest NP concentration. Similarly to the water case, comparing these

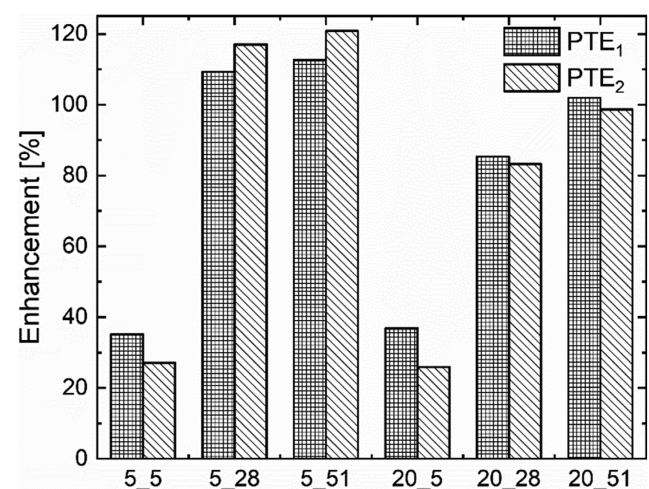


Figure 9. PTE enhancement of NFs in relation to water.

results to the PTE enhancements for the water-based Au NFs obtained in previous studies is a difficult task. The references in Table 1, which also cover different experimental setups, calculation procedures, light sources, and NP sizes and concentrations, provide a wide range of enhancement variations (from 11% to 518%). To help to advance the potential ability of solar NFs for DASC, it is necessary to do away with the inconsistencies in these PTE enhancement results. Round robin tests have been used in the past to overcome the high dispersion of results in other NFs variables, such as thermal conductivity,^[43,44] specific heat capacity,^[45] contact angle,^[46] numerical simulation,^[47] etc. They might help in this case.

3.5. PTE Statistical Analysis

The experimental data collected for PTE were statistically analyzed. The methodology followed for the statistical analyses is depicted in **Figure 10**. The analyses started with an initial normality check by the Shapiro Wilk test,^[48] along with the homogeneity of variances assumptions and some descriptive data statistics. Parametric tests are used if data exhibit normal distribution, and nonparametric tests otherwise. A comparison of the differences between the mean ranks of the independent groups of the normally distributed variables was performed by independent samples, with T-tests and analysis of variances (ANOVA's) when there were two groups or more, respectively.^[49] The Kruskal–Wallis test was employed when the normal distribution assumption was not valid.^[50]

The statistical analyses were followed with the PTE variation based on the independent variables (Au NP concentration, [Au] and NP size, *D*). As the normal distribution assumption was not valid in this case, the Kruskal–Wallis test was run to investigate the differences between the means of the PTE trends based on the *D* groups. The results are provided in **Table 6**.

The mean rank values of the PTE measurements were statistically different based on the *D* groups ($p < 0.05$). For the different *D* values (0, 5, 20 nm), the PTE values significantly changed. A post hoc Bonferroni analysis was run to determine the group/groups of *D* that brought about this difference. The results showed that the difference between the mean rank values of PTE was statistically significant for the *D* = 0 nm (water) and

Table 6. Comparison of the means of the PTE values based on the NP size (*D*) groups.

	<i>D</i> [nm]	<i>n</i>	Mean	Standard deviation	Mean Rank	Test statistics	<i>p</i>
PTE [%]	0	4	22.390	1.181	2.50	11.312 ^{b)}	0.003 ^{a)}
	5	8	43.983	9.967	13.44		
	20	6	37.903	7.695	8.92		

^{a)} $p < 0.05$; ^{b)}Kruskal–Wallis test.

Table 7. Comparison of the means of the PTE values based on the NP concentration [Au] groups.

	[Au] [ppm]	<i>n</i>	Mean	Standard Deviation	Test Statistics	<i>p</i>
PTE [%]	0	4	22.390	1.181	66.701 ^{b)}	0.000 ^{a)}
	5.1	4	28.323	0.236		
	28.2	4	44.813	4.684		
	51.3	6	47.790	3.913		

^{a)} $p < 0.05$; ^{b)}ANOVA test.

D = 5 nm groups ($p = 0.002$). The *D* = 5 nm group obtaining higher PTE mean values than those of *D* = 0 nm (water). All the other comparisons were statistically insignificant (i.e., between *D* = 5 and 20 nm, and between *D* = 0 and 20 nm).

To determine the differences between the means of the PTE trends based on the [Au] groups, the ANOVA test was used because data exhibited normal distribution and more than two groups were present. The results are provided in **Table 7**.

The results in Table 7 revealed that the difference in the mean PTE measurement values was statistically significant based on the [Au] groups ($p < 0.05$). The post hoc Bonferroni analysis showed that the [Au] = 0 ppm (water) group's PTE mean statistically differed from those of the [Au] = 28.2 ppm and [Au] = 51.3 ppm groups ($p = 0.000$, $p = 0.000$). [Au] = 0 ppm gave a lower PTE mean value than the [Au] = 28.2 ppm and [Au] = 51.3 ppm groups. The differences between the mean PTE values of [Au] = 5.1 ppm and [Au] = 28.2 ppm, and

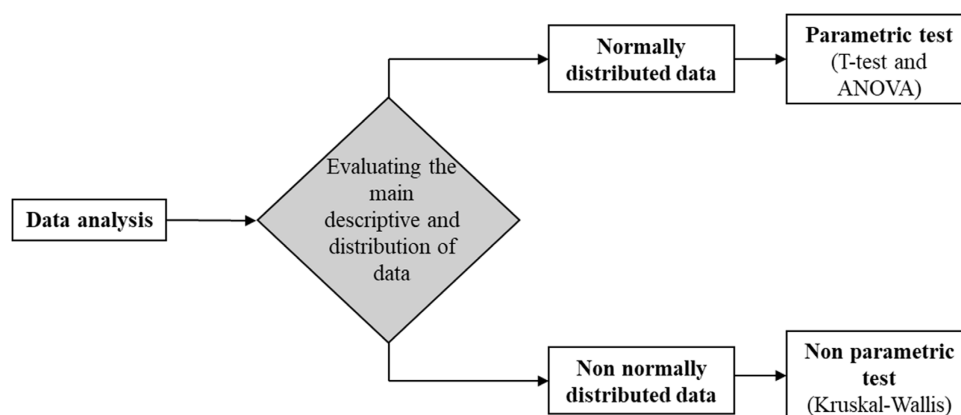


Figure 10. The statistical methodology of this study.

Table 8. Correlation analysis between the independent ([Au], D) and dependent (PTE) variables (p : significance value, ρ : correlation coefficient).

		PTE
D	p	0.305
	ρ	0.199
[Au]	p	0.000 ^{a)}
	ρ	0.770

^{a)} $p < 0.05$.

[Au] = 5.1 ppm and [Au] = 51.3 ppm were statistically significant ($p = 0.000$, $p = 0.000$). [Au] = 51.3 ppm gave the highest PTE mean value.

The correlation between the [Au] and D (ordinal) categorical and the PTE continuous variables was studied by Kendall's Tau correlation, applied for normally distributed data. The results in **Table 8** indicate that the correlations between D -PTE were not statistically significant ($p > 0.05$). This implies that these variable pairs were not statistically associated with one another. The correlation between [Au]-PTE was statistically significant ($p < 0.05$), with a correlation coefficient between those two variables of 0.770 (> 0.60), indicating a positive strong correlation.^[51]

4. Conclusions

Gold, one of the metal materials that presents SPR, is a good candidate to improve the solar radiation absorption capacity of solar NFs using this property. The suitability of water-based Au NFs to be used in DASC was herein studied. Different particle sizes of 5 and 20 nm, and Au concentrations of 5.1, 28.2, and 51.3 ppm, were applied to evaluate the effect of these variables on the study of several properties related to DASC photothermal performance. Some important conclusions can be drawn: 1) Commercial Au NFs of both sizes show good colloidal stability at the maximum temperatures reached during the PTE experiments (below 40 °C); 2) The extinction coefficient measurements reveal that NFs have an advantage over water for absorbing solar radiation at wavelengths within the visible radiation spectrum; 3) For the employed Au NP sizes, NFs presented a plasma resonance wavelength at 516 and 520 nm for 5 and 20 nm, respectively. This wavelength was independent of the concentration and increases with NP size; 4) The influence of particle size on the extinction coefficient is not relevant compared to the Au concentration. The best result is obtained for the NFs at the 51.3 ppm concentration; 5) A positive effect on the fraction of absorbed sunlight with the addition of NPs appears, and the penetration distance at which light is absorbed significantly reduces. All this is important for reducing dimensions and costs when designing DASC; 6) Two methods were used to calculate PTE. The first one does not consider heat losses, but the second calculation method does. Although the absolute values of both PTE calculations differ, PTE enhancements in relation to water show similar trends in both cases; 7) Enhanced PTE takes place

for all the tested NFs. The maximum 121% PTE enhancement in relation to the base fluid is obtained for the NF with 5 nm NPs at the 51.3 ppm concentration; 8) A statistical analysis can be used to evaluate the influence of the input variables on the PTE results. It confirms that NP size (D) and Au concentration ([Au]) statistically and significantly influence PTE; 9) For the entire dataset, the correlations between D -PTE are not statistically significant. So these variable pairs are not statistically associated with one another, while the correlations between [Au]-PTE are statistically significant, positive, and strong; 10) Although the Au concentration positively impacts PTE, the increase in PTE within the measured concentration range is not linear. A threshold is obtained beyond which no further improvement can be achieved; and 11) Given the high dispersion of the PTE present in the literature, comparing the results to previous works is not easy. A round-robin test might be interesting to overcome this high dispersion and to help to advance in the potential application of solar NFs in DASC.

From the future DASC industrial application point of view, the results in this article highlight the advantage of using smaller sized NPs (thanks to the lower Au concentration improving the PTE results) and the reduction in the required NF volume to reduce collector depth. Both have a positive effect on the DASC cost.

Supporting Information

Supporting Information is available from the Wiley Online Library or from the author.

Acknowledgements

This research was partially funded by the Generalitat Valenciana through Project PROMETEO/2020/029 and by the Universitat Jaume I through Project UJI-B2020-32.

Conflict of Interest

The authors declare no conflict of interest.

Data Availability Statement

The data that support the findings of this study are available from the corresponding author upon reasonable request.

Keywords

gold nanoparticles, optical properties, photothermal conversion efficiency, solar nanofluids, statistical analysis

Received: February 1, 2022
Revised: March 17, 2022
Published online: April 4, 2022

[1] J. Delbeke, A. Runge-Metzger, Y. Slingenberg, J. Werksman, *Towards a Climate-Neutral Europe. Courbing the Trend*, Taylor and Francis Group, London 2019, pp. 24–45.

- [2] Z. Aqachmar, H. Ben Sassi, K. Lahrech, A. Barhdadi, *Int. J. Hydrogen Energy* **2021**, 46, 30790.
- [3] J. E. Minardi, H. N. Chuang, *Sol. Energy* **1975**, 17, 179.
- [4] R. A. Rasih, N. A. C. Sidik, S. Samion, *J. Therm. Anal. Calorim.* **2019**, 137, 903.
- [5] S. U. S. Choi, J. A. Eastman, in *Proc. ASME Int. Mechanical Engineering Congress and Exhibition*, San Francisco, November **1995**, <https://www.osti.gov/servlets/purl/196525>.
- [6] X.-Q. Wang, A. S. Mujumdar, *Int. J. Therm. Sci.* **2007**, 46, 1.
- [7] M. M. Tawfik, *Renewable Sustainable Energy Rev.* **2016**, 75, 1239.
- [8] A. Arshad, M. Jabbar, Y. Yan, D. Reay, *J. Mol. Liq.* **2019**, 279, 444.
- [9] E. C. Okonkwo, I. Wole-Osho, I. W. Almanassra, Y. M. Abdullatif, T. Al-Ansari, *J. Therm. Anal. Calorim.* **2021**, 145, 2817.
- [10] T. P. Otanicar, P. E. Phelan, J. S. Golden, *Sol. Energy* **2009**, 83, 969.
- [11] R. Taylor, S. Coulombe, T. Otanicar, P. Phelan, A. Gunawan, W. Lv, G. Rosengarten, R. Prasher, H. Tyagi, *J. Appl. Phys.* **2013**, 113, 011301.
- [12] Tahereh B. Gorji, A.A. Ranjbar, *Renewable Sustainable Energy Rev.* **2017**, 72, 10.
- [13] E. P. Bandarra Filho, O. S. H. Mendoza, C. L. L. Beicker, A. Menezes, D. Wen, *Energy Convers. Manag.* **2014**, 84, 261.
- [14] H. Zhang, H.-J. Chen, X. Du, D. Wen, *Sol. Energy* **2014**, 100, 141.
- [15] A. Zeiny, H. Jin, L. Bai, G. Lin, D. Wen, *Sol. Energy* **2018**, 161, 74.
- [16] H. Zhang, H.-J. Chen, X. Du, G. Lin, D. Wen, *J. Nanosci. Nanotechnol.* **2015**, 15, 3055.
- [17] M. Chen, Y. He, J. Huang, J. Zhu, *Energy Convers. Manag.* **2016**, 127292.
- [18] M. Chen, Y. He, J. Zhu, D. R. Kim, *Energy Convers. Manag.* **2016**, 112, 21.
- [19] H. Jin, G. Lin, L. Bai, M. Amjad, E. P. Bandarra Filho, D. Wen, *Sol. Energy* **2016**, 139, 278.
- [20] H. Jin, G. Lin, L. Bai, A. Zeiny, D. Wen, *Nano Energy* **2016**, 28, 397.
- [21] M. Chen, Y. He, J. Huang, J. Zhu, *Int. J. Heat Mass Transf.* **2017**, 108, 1894.
- [22] X. Wang, Y. He, X. Liu, L. Shi, J. Zhu, *Sol. Energy* **2017**, 157, 35.
- [23] Y. He, M. Chen, X. Wang, Y. Hu, *Sol. Energy* **2018**, 171, 73.
- [24] T. Yousefi, F. Veysi, E. Shojaeizadeh, S. Zinadini, *Renewable Energy* **2012**, 39 293.
- [25] Z. Said, R. Saidur, N.A. Rahim, *Int. Commun. Heat Mass Transf.* **2014**, 59, 46.
- [26] H. K. Gupta, G. D. Agrawal, J. Mathur, *Sol. Energy* **2015**, 118, 390.
- [27] D. Han, Z. Meng, D. Wu, C. Zhang, H. Zhu, *Nanoscale Res. Lett.* **2011**, 6, 1.
- [28] S. Delfani, M. Karami, M. A. A. Behabadi, *Renewable Energy* **2016**, 87, 754.
- [29] E. Sadeghinezhad, M. Mehrali, R. Saidur, M. Mehrali, S. Tahan Latibari, A. R. Akhiani, H. S. C. Metselaar, *Energy Convers. Manag.* **2016**, 111, 466.
- [30] T. Aguilar, E. Sani, L. Mercatelli, I. Carrillo-Berdugo, E. Torres, J. Navas, *J. Mol. Liq.* **2020**, 306, 112862.
- [31] X. Wang, Y. He, M. Chen, Y. Hu, *Sol. Energy Mater. Sol. Cells* **2017**, 179, 185.
- [32] L. Wang, G. Zhu, M. Wang, W. Yu, J. Zeng, X. Yu, H. Xie, Q. Li, *Sol. Energy* **2019**, 184, 240.
- [33] X. Li, G. Zeng, X. Lei, *Sol. Energy Mater. Sol. Cells* **2020**, 206, 110323.
- [34] H. Wang, W. Yang, L. Cheng, C. Guan, H. Yan, *Sol. Energy Mater. Sol. Cells* **2017**, 176, 374.
- [35] X. Zuo, W. Yang, M. Shi, H. Yan, C. Guan, S. Wu, Z. Zhang, X. Li, Z. Li, *Sol. Energy* **2021**, 218, 1.
- [36] A. Kosinska, B. V. Balakin, P. Kosinski, *AIP Adv.* **2021**, 11, 055214.
- [37] M. Rycenga, C. M. Cobley, J. Zeng, W. Li, C. H. Moran, Q. Zhang, D. Qin, Y. Xia, *Chem. Rev.* **2011**, 111, 3669.
- [38] B. Kamenik, E. B. Elcioglu, A. Turgut, R. Mondragón, L. Hernandez Lopez, J.P. Vallejo, L. Lugo, M.H. Buschmann, J. Ravnik, *Int. J. Thermofluids* **2022**, 14, 100144.
- [39] E. Sani, S. Barison, C. Pagura, L. Mercatelli, P. Sansoni, D. Fontani, D. Jafrancesco, F. Francini, *Opt. Express* **2010**, 18 5179.
- [40] E. Sani, L. Mercatelli, S. Barison, C. Pagura, F. Agresti, L. Colla, P. Sansoni, *Sol. Energy Mater. Sol. Cells* **2011**, 95 2994.
- [41] *Standard Tables for Reference Solar Spectral Irradiances: Direct Normal and Hemispherical on 37° Tilted Surface*, ASTM International **2012**, p. G 173-03, <https://standards.globalspec.com/std/3848322/astm-g173-03-2012>.
- [42] A. Gimeno-Furió, R. Martínez-Cuenca, R. Mondragón, A. F. V. Gasulla, C. Doñate-Buendía, G. Mínguez-Vega, L. Hernández, *Energy* **2020**, 212, 118763.
- [43] J. Buongiorno, D. C. Venerus, N. Prabhat, T. Mckrell, J. Townsend, R. Christianson, Y. V. Tolmachev, P. Keblinski, L.-W. Hu, J. L. Alvarado, I. C. Bang, S. W. Bishnoi, M. Bonetti, F. Botz, A. Cecere, Y. Chang, G. Chen, H. Chen, S. J. Chung, M. K. Chyu, S. K. Das, R. Di Paola, Y. Ding, F. Dubois, G. Dzido, J. Eapen, W. Escher, D. Funfschilling, Q. Galand, J. Gao, et al., *J. Appl. Phys.* **2009**, 106, 094312.
- [44] W.-H. Lee, C.-K. Rhee, J. Koo, J. Lee, S. P. Jang, S. U. S. Choi, K.-W. Lee, H.-Y. Bae, G.-J. Lee, C.-K. Kim, S. W. Hong, Y. Kwon, D. Kim, S. H. Kim, K. S. Hwang, H. J. Kim, H. J. Ha, S.-H. Lee, C. J. Choi, J.-H. Lee, *Nanoscale Res. Lett.* **2011**, 6 1.
- [45] B. Muñoz-Sánchez, J. Nieto-Maestre, J. González-Aguilar, J. E. Julia, N. Navarrete, A. Faik, T. Bauer, A. Bonk, M. E. Navarro, Y. Ding, N. Uranga, E. Veca, S. Sau, P. Giménez, P. García, J. I. Burgaleta, *AIP Conf. Proc.* **2017**, 1850, pp. 080017.
- [46] M. Hernaiz, V. Alonso, P. Estellé, Z. Wu, B. Sundén, L. Doretta, S. Mancin, N. Çobanoğlu, Z.H. Karadeniz, N. Garmendia, M. Lasheras-Zubieta, L. Hernández López, R. Mondragón, R. Martínez-Cuenca, S. Barison, A. Kujawska, A. Turgut, A. Amigo, G. Huminic, A. Huminic, M.-R. Kalus, K.-G. Schroth, M.H. Buschmann, *J. Colloid Interface Sci.* **2019**, 547, <https://doi.org/10.1016/j.jcis.2019.04.007>.
- [47] A. A. Minea, B. Buonomo, J. Burggraf, D. Ercole, K. R. Karpaiya, A. Di Pasqua, G. Sekrani, J. Steffens, J. Tibaut, N. Wichmann, P. Farber, A. Huminic, G. Huminic, R. Mahu, O. Manca, C. Oprea, S. Poncet, J. Ravnik, *Int. Commun. Heat Mass Transf.* **2019**, 108, 104292.
- [48] N. M. Razali, Y. B. Wah, *J. Stat. Model. Anal.* **2011**, 2, 21.
- [49] P. Mishra, U. Singh, C. M. Pandey, P. Mishra, G. Pandey, *Ann. Card. Anaesth.* **2019**, 22, 407.
- [50] D. J. Sheskin, *International Encyclopedia of Statistical Science* (Ed: M. Lovric), Springer, Berlin, Heidelberg **2011**.
- [51] S. B. Gerber, K. V. Finn, *Using SPSS for Windows Data Analysis and Graphics*, 2nd ed., Springer Science + Business Media, Inc., New York **2005**.